

Efficient Modeling of Time-domain AEM using Finite-volume Method

Xiuyan Ren¹, Changchun Yin^{1*}, Yunhe Liu¹, Jing Cai¹, Cong Wang¹ and Fang Ben²

¹College of Geo-exploration Sciences and Technology, Jilin University, China, 130026

²Institute of Geophysical and Geochemical Exploration, China Academy of Geological Science, Langfang, 065000, China

*Corresponding author; Email: yinchangchun_jlu@163.com

ABSTRACT

We present an efficient three-dimensional (3D) time-domain airborne electromagnetic (EM) modeling based on finite-volume method, in combination with the merits of solving the secondary field, local mesh, and the direct solver. Taking the strategy of separating primary from secondary field for the calculation of time-domain EM field, we greatly reduce the number of grids in comparison to direct solution of the total field. The primary field is obtained by Hankel transform from the frequency-domain for a half-space or layered earth model. The techniques of local mesh and direct solver are adopted to further improve the modeling efficiency. We compare and discuss the characteristics of the method developed in this paper from time consumption and grid sizes. The EM responses for different transmitting waveforms are calculated via a convolution between step-wave responses and the transmitting current or its derivatives. All numerical experiments on models with multiple geological bodies and fracture zones have demonstrated that our modeling algorithm is efficient and effective when simulating AEM system responses.

Introduction

The airborne EM (AEM) methods have been used for mineral exploration, geological mapping for years. Concurrently, the forward modeling and inversion techniques are being developed. There are many algorithms for time-domain AEM modeling and the main stream includes transformation from the frequency-domain, the explicit method such as time-domain finite difference (FDTD), and the implicit method. For the transformation method, the frequency-domain response is conventionally solved for the secondary electric or magnetic field. This is done because the frequency-domain primary field can be easily separated from secondary field and the secondary field has a small footprint, leading to less computation. Furthermore, there exists the singularity at the transmitting source, which can cause numerical errors in the calculation of total EM field. The time-domain response is obtained very fast via Fourier transform from frequency-domain and it is generally very stable for simple electric structures like one-dimensional (1D) earth. Zhu *et al.* (2010) used G-S inverse Laplace transform to obtain time-domain helicopter-borne EM data for conductivity-depth imaging. Sasaki and Cho (2011) presented an

efficient three-dimensional (3D) time-domain EM modeling, in which they first used the frequency-domain finite-difference formulation on a staggered grid and then transformed the results to time-domain using sine and cosine digital filters. Yin *et al.* (2013) calculated the one-dimensional (1D) time-domain full-time EM responses based on Hankel transform and the convolution algorithm (Yin *et al.*, 2015). The explicit calculation methods, like FDTD, typically obtain the time-domain responses iteratively from a starting EM field. It was developed by Wang and Hohmann (1993), and Commer and Newman (2004) presented a similar algorithm. Xu *et al.* (2012) conducted a 3D full-waveform airborne EM calculation with FDTD, and Zhao *et al.* (2015) studied the topographic effect on airborne EM based on FDTD method. However, to guarantee the convergence, FDTD has a rigorous constraint condition on the time and space steps. While the implicit method weakens the condition, the development of direct solver further speeds up the computation when comparing with the iterative method. The latter requires many iterations for each time step, resulting in large amounts of computation, especially for AEM modeling. Oldenburg *et al.* (2008, 2013) presented a direct calculation of time-domain EM field by using direct solver for large-scale multi-source transient EM

problems, where they used a finite-volume (FV) technique in space and backward Euler in time to discretize the Maxwell's equations. With a direct solver, they only need to factorize the coefficient matrix once and replace the source term for the same time step. This saves considerably the time in forward modeling and inversion. However, though the direct solver has its advantages, for very large problems the memory requirement and the communication time between processors also become **prohibitively** high. Yang *et al.* (2013) developed a generic parallelization scheme in the **diffusive regime** with locally optimized meshes, where the local mesh has a small scale with fine cells near the transmitting source and sounding stations and coarse cells in far area in accordance with EM diffusion and the geometric decay of the signals. Cox and Zhdanov (2007, 2010) proposed the moving footprint concept that greatly speeds up 3D EM calculation. All these methods are aimed at enhancing the modeling accuracy and reducing the computing time.

In this paper, we adopt the FV method with staggered grids for space discretization. From numerical simulations point view, the finite-difference (FD) method is a differential process that uses the difference to replace the derivative, while the FV is an integral process in every controlled volume that divides the whole region without overlap. The finite-element (FE) is a widely-used numerical method that uses the combination of interpolation function and node values in each subdivided element to express the variables and solves the equation based on a variational principle or weighted residual method. Compared with FE, FV possesses the conservation property of variables in every controlled volume and has simpler computation process. Yang *et al.* (2012) used FV method to conduct 3D frequency-domain marine controlled-source EM (MCSEM) topographic modeling. Oldenburg *et al.* (2013) made 3D multisource time-domain EM inversion, in which they use FV with staggered grids to discretize the equations. However, their algorithm handles the total-field. Jahan-dari and Farquharson (2014) used FV method to solve the frequency-domain EM forward problem with unstructured grids, where they discretized the Helmholtz equation for the electric field and used the edge vector interpolation functions to compute the electric and magnetic fields.

In this paper, we use separation method with FV to deal with the secondary field modeling for time-domain airborne EM, in which EM field for a homogeneous half-space is used as the primary field. We first establish the time-domain electric field equation and adopt FV method to make space

discretization for the secondary electric field and the implicit Euler formula for time discretization. We then combine the merits of solving the secondary field, local mesh and direct solver together to conduct a time-domain airborne EM 3D modeling. The MPI is used in factorization procedure. We show accuracy and efficiency by comparing our algorithm with those solving the total field from grid size and time consumption. Finally, we demonstrate the feasibility of our method via numerical experiments for different transmitting waves and complex underground structures.

Separation Method

Equations for Secondary EM Field

The forward modeling in time-domain AEM starts from the following Maxwell's equations

$$\nabla \times \mathbf{E} + \mu \frac{\partial \mathbf{H}}{\partial t} = 0, \quad (1)$$

$$\nabla \times \mathbf{H} - \sigma \mathbf{E} - \varepsilon \frac{\partial \mathbf{E}}{\partial t} = \mathbf{S}(r, t), \quad (2)$$

where \mathbf{E} and \mathbf{H} are respectively the electric and magnetic field, the transmitting source is $\mathbf{S}(r, t)$, σ , ε and μ are the conductivity, **dielectric permittivity** and magnetic permeability, respectively. We assume the permeability of the subsurface to be that of free-space μ_0 . Using \mathbf{E}_p , \mathbf{H}_p and \mathbf{E}_s , \mathbf{H}_s to **denote** the primary field and secondary field, respectively, the total EM field is then expressed as

$$\mathbf{E} = \mathbf{E}_p + \mathbf{E}_s, \quad (3)$$

$$\mathbf{H} = \mathbf{H}_p + \mathbf{H}_s. \quad (4)$$

Running a simple transform on Eqs. (1) through (4) and ignoring the **displacement current**, we obtain the control equations for the secondary electric field, *i.e.*,

$$\nabla \times \nabla \times \mathbf{E}_s + \mu \sigma \frac{\partial \mathbf{E}_s}{\partial t} = -\mu(\sigma - \sigma_p) \frac{\partial \mathbf{E}_p}{\partial t} \quad (5)$$

where σ_p is the background half-space conductivity.

Assuming V is a control volume and ∂V is its surface, the Gaussian divergence theorem can be expressed by the following identical equation,

$$\iiint_V \nabla \times \mathbf{F} dV = \iint_{\partial V} \mathbf{n} \times \mathbf{F} dS. \quad (6)$$

We transform the volume integral into surface integral, so Eq. (5) becomes

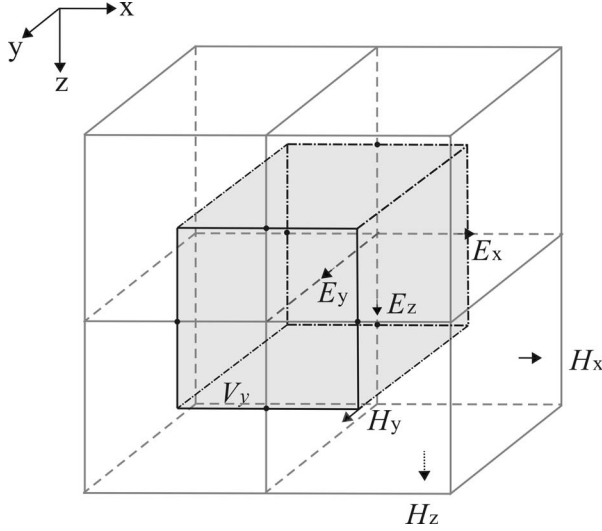


Figure 1. **E** and **H** field in the staggered grid. V_y is the control volume for E_y .

$$\begin{aligned} \iiint_V \mu \sigma \frac{\partial \mathbf{E}_s}{\partial t} dV + \iint_{\partial V} \mathbf{n} \times (\nabla \times \mathbf{E}_s) dS \\ = - \iiint_V \mu (\sigma - \sigma_p) \frac{\partial \mathbf{E}_p}{\partial t} dV, \end{aligned} \quad (7)$$

where \mathbf{n} is the unit normal vector of ∂V . We employ Yee's grids (Yee, 1996) to discretize Eq. (7), where \mathbf{E} is assumed to be in the middle of the edge, while \mathbf{H} is at the center of each surface. For each field component, there exists a control volume around it, as shown in Fig. 1. To simplify the expression, we use several operators to rewrite Eq. (7) as

$$G^V C \frac{\partial \mathbf{E}_s(t)}{\partial t} + G^{\partial V} \mathbf{D} \mathbf{E}_s(t) = -G^V J_r \frac{\partial \mathbf{E}_p(t)}{\partial t}, \quad (8)$$

where G^V and $G^{\partial V}$ are respectively the volume and surface integration operator, C is the product of conductivity and permeability, D is the cross product operator of outer normal vector of surface and the curl of vector field, and J_r is the product of permeability and anomalous conductivity.

For time discretization, we adopt the backward Euler (BE) scheme. The BE method with long time steps ignore the wavy part altogether and skips to the diffusive part without significant loss of accuracy (Haber, 2014). We employ Taylor expansion and make an approximation to obtain the second-order formula (Um et al., 2010):

$$\frac{\partial \mathbf{E}_s(t)}{\partial t} = \frac{1}{2\Delta t} (3\mathbf{E}_s^{i+1} - 4\mathbf{E}_s^i + \mathbf{E}_s^{i-1}). \quad (9)$$

Combining with the space discretization, we obtain the complete discretized equation, i.e.,

$$\begin{aligned} (3G^V C + 2\Delta t G^{\partial V} \mathbf{D}) \mathbf{E}_s^{i+1} \\ = G^V C (4\mathbf{E}_s^i - \mathbf{E}_s^{i-1}) - G^V J_r (3\mathbf{E}_s^{i+1} - 4\mathbf{E}_s^i + \mathbf{E}_s^{i-1}), \end{aligned} \quad (10)$$

where Δt is the time step, $i+1$, i , and $i-1$ represent adjacent time channels. This indicates that the secondary field at $i+1$ moment is induced by the fields of two previous moments and the background field at the present time. Since the time has a very large range, an equal time step can result in unacceptable computational cost. Considering the **propagation characteristics** that the electric field decays fast at early time and slowly at later time, we choose a time step for each order of logarithmic time, which guarantees the small steps in early time but large ones in late time.

Primary Electric Field

To solve the secondary electric field, we need to first calculate the primary field. We employ the **semi-analytic** solution for a half-space to calculate the primary electric field. The electric field is first calculated in frequency-domain,

$$\begin{aligned} E_{px}^i = \frac{m}{2\pi R} \int_0^\infty \left(F_i^+ e^{-u_i(z-z_i)} + F_i^- e^{-u_i(z_{i+1}-z)} \right) \\ \times \lambda^2 J_1(\lambda R) d\lambda, \end{aligned} \quad (11)$$

$$\begin{aligned} E_{py}^i = -\frac{m}{2\pi R} \int_0^\infty \left(F_i^+ e^{-u_i(z-z_i)} + F_i^- e^{-u_i(z_{i+1}-z)} \right) \\ \times \lambda^2 J_1(\lambda R) d\lambda, \end{aligned} \quad (12)$$

where m is the transmitting dipole moment, R is the distance between the transmitter and the receiver, F_i^+ and F_i^- are amplitudes of EM waves propagating respectively downwards and upwards in the i^{th} layer, u_i is related to the wave number of the i^{th} layer, z_i and z_{i+1} are respectively the top and bottom interface of i^{th} layer, while J_1 is Bessel's function of the first-order. We calculate the frequency-domain primary electric field at the interface of each layer along the radial direction and use 8 values along the radius (4 on each side) to interpolate the field to the grids. The time-domain electric field at all edges for all time steps can be calculated by a cosine transform

$$f(t) = -f_{DC} + \frac{2}{\pi} \int_0^{+\infty} \text{Re}[F(\omega)] \cos \omega t d\omega, \quad (13)$$

where $\text{Re}[F(\omega)]$ is the real part of the field in the frequency-domain, while f_{DC} is the DC field that can be

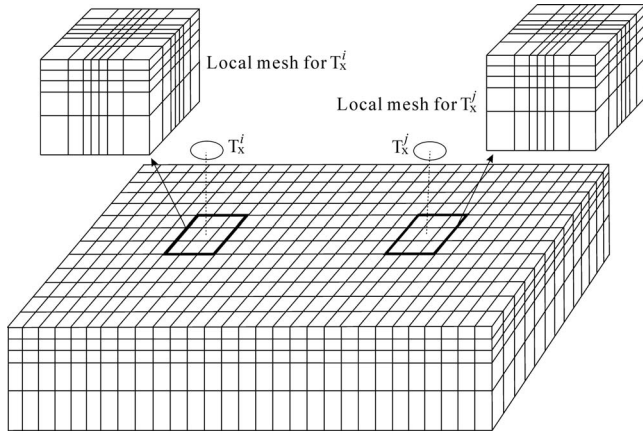


Figure 2. Local mesh for transmitters T_x^i and T_x^j .

assumed to be zero for a magnetic transmitting dipole. The cosine transform can be evaluated using the digital filtering technique (Christensen, 1990). We store the time-domain primary field for reuse in other models if the same background model is assumed. For the AEM system with a large transmitting loop, we can divide the loop into a series of the magnetic dipoles and calculate the electric field by totaling their contributions.

Initial Conditions and Boundary Conditions

For the step-off transmitting wave, the initial electric and magnetic fields satisfy

$$\mathbf{E}_p(\mathbf{r}, 0) = 0, \quad (14)$$

$$\mathbf{E}_s(\mathbf{r}, 0) = 0, \quad (15)$$

$$\mathbf{H}_p(\mathbf{r}, 0) = \mathbf{H}_0, \quad (16)$$

where the magnetic field has an initial static value \mathbf{H}_0 . We assume the homogenous Dirichlet boundary condition, and in the infinity we assume the tangential electric field to be zero. The boundary conditions are written as

$$\mathbf{n} \times \mathbf{E}_s = 0 \quad \text{at } \partial V', \quad (17)$$

where $\partial V'$ denotes the outside boundary of the entire model region.

Solution to the Forward Problem

Airborne EM modeling problem is a multi-source and multi-channel problem, a direct solver can be a good choice for the solution, because it makes coefficient matrix factorization only once for all sources and the same time step. Also, the solution of equations system using direct solvers is virtually independent of the condition number of the coefficient matrix (Operto *et al.*, 2007; Jahandari and Farquharson, 2014). For the

problem of $\mathbf{Ax} = \mathbf{b}$, we adopt the software package MUMPS (Multi-frontal Massive Parallel Solver) developed by the CERFACS group (Amestoy *et al.*, 2001) for the solution of the discretized equation. MUMPS uses a multi-frontal technique that is a direct method based on either the LU or LDL^T factorization of the coefficient matrix (Oldenburg *et al.*, 2013). However, solving the whole survey area with a global mesh that contains all the sounding stations and produces many unnecessary fine grids can result in a huge number of unknowns and very large memory requirements. Actually, airborne EM has a small sensitive area (footprint) especially for the secondary field. To make use of the merit of direct solver while avoiding the large memory requirement, we bring in local mesh that allows for a large EM problem to be decomposed into many small highly-independent ones (Yang *et al.*, 2013). The local mesh is located below the transmitter and the grids are refined near the source and coarse far away from it, as shown in Fig. 2. We make use of local mesh that requires less grids and direct solver that needs one factorization for the same time steps, for the solution of the discretized equation. In this way, we can effectively obtain the secondary electric field at all the edges of the grids.

Discretizing Eq. (1), we can interpolate the magnetic induction $d\mathbf{H}_s/dt$ at the receiver location from the secondary electric field, and the magnetic field can be obtained by integration. After obtaining the secondary field, we add the primary and the secondary field together for the total field.

Accuracy Check and Efficiency Analysis

We assume a geological body of 200 m×200 m×40 m with a resistivity of 1 $\Omega\cdot\text{m}$ and a depth of 60 m embedded in a homogeneous half-space of 100 $\Omega\cdot\text{m}$. The air resistivity is $10^6 \Omega\cdot\text{m}$. We take as example an concentric AEM system with the flight height of 30 m, the transmitter loop has a diameter of 26 m and the step transmitting current has an amplitude of 10 A (Fig. 3). We design a local mesh (local mesh 1) centered at the middle of the transmitter loop with a dimension of 200 m×200 m×200 m and an extension of 280 m on each side in horizontal directions and 1,000 m extension in the vertical direction. The time channel from 10^{-6} s to 0.1 s is divided into five logarithmically-equal intervals with each subdivided into 100 equal time steps. Five factorizations and 500 forward models are pursued. We conduct the computation on a work station with Intel(R) Xeon(R) CPU E5-2650 v3 @2.30GHz and 128GB memory.

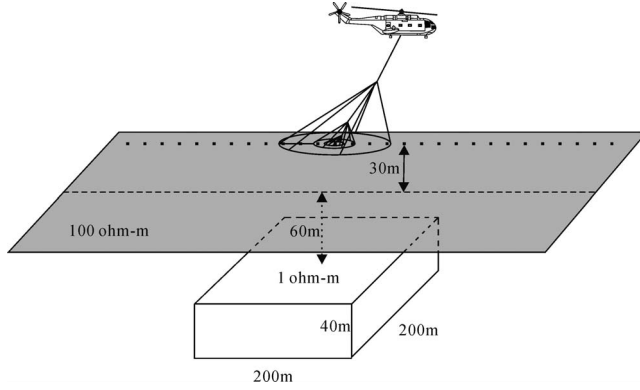


Figure 3. A 3D conductive body embedded in a homogeneous half-space.

To demonstrate the accuracy and efficiency of this method, we first calculate the EM response using unstructured FE method by Yin *et al.* (2016), in which the region has been divided into 222,527 grids (257,991 unknowns) with many fine cells near the source, the air-earth surface and the geological target to guarantee good results, and then we respectively use the method of this paper and a total-field method to calculate the EM response from the same local mesh 1 ($16 \times 16 \times 30$). The total-field method is derived directly from the Maxwell equations without field separation. The comparison of the results from all three algorithms is shown in Fig. 4. From the figure, one can see that the responses of our method agree well with the unstructured FE results, however, the total-field method with the same mesh delivers inaccurate results. To reach the same accuracy level, we have to extend the mesh for the total-field

method from local mesh 1 to grid size of $24 \times 24 \times 37$ (local mesh 2). Figure 4 shows that the results of total-field method with local mesh 2 agree well with those of the other two methods. From Fig. 4, we conclude that with the same grids, our algorithm has higher accuracy. To obtain the same accuracy for AEM modeling, our method requires fewer grids than the total-field method.

To further demonstrate the **feasibility** of our method, we carry out a profile calculation for the same model as in Fig. 3. The target region sets 47 transmitter locations along the profile at the interval of 20 m. Figure 5 shows the consistency of two methods for different time channels, where the solid lines and diamonds are respectively for the results of our method with local mesh 1 and the total-field method with local mesh 2. From Fig. 5, one sees that for an embedded conductive geological body, dB_z/dt shows an anomaly varies from the negative value in the early time to the positive one with time, while B_z keeps a positive anomaly.

Table 1 gives the time consumption for the total-field method and the separation method of this paper. In this table, t_f and t_s represent the time for one factorization and one solving procedure; n_f is the number of factorization for one transmitter; n_s is the number of solving process for one transmitter; N_{tx} is the number of transmitters. One sees that for one factorization and one solving procedure, the separation method costs 0.7 s and 0.02 s, respectively, reducing time by 83.33% and 71.43% compared to the total-field method. For the whole profile, the total running time is speeded up by 75.9%. We can expect that if only very limited time channels are to be calculated, the total time consumption

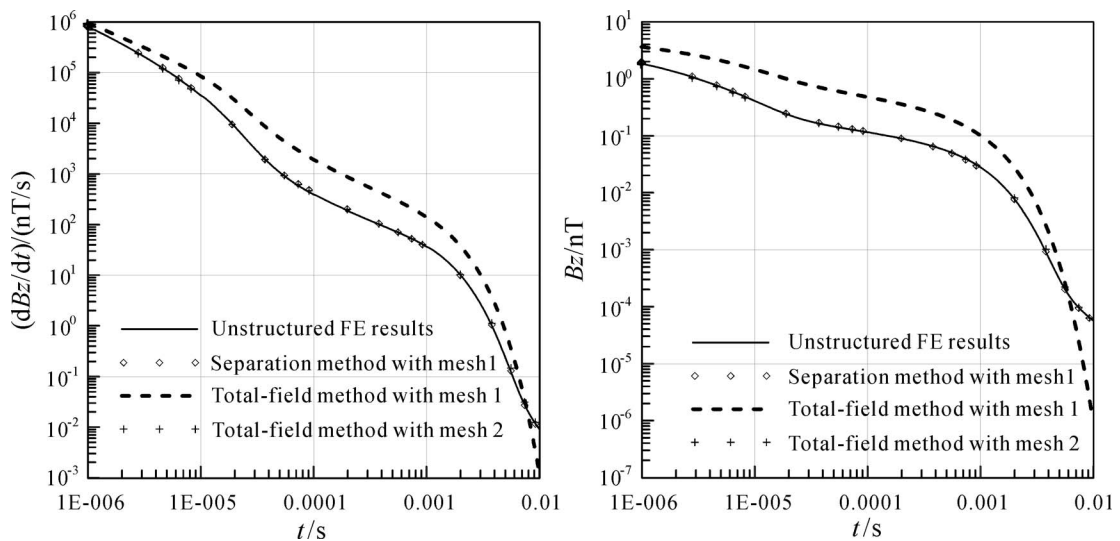


Figure 4. Comparison of the separation method of this paper with other methods. The EM system is above the center of the geological body. Note that the separation method has the same accuracy as FE. To reach the same accuracy level, however, the total-field method has to use a larger mesh.

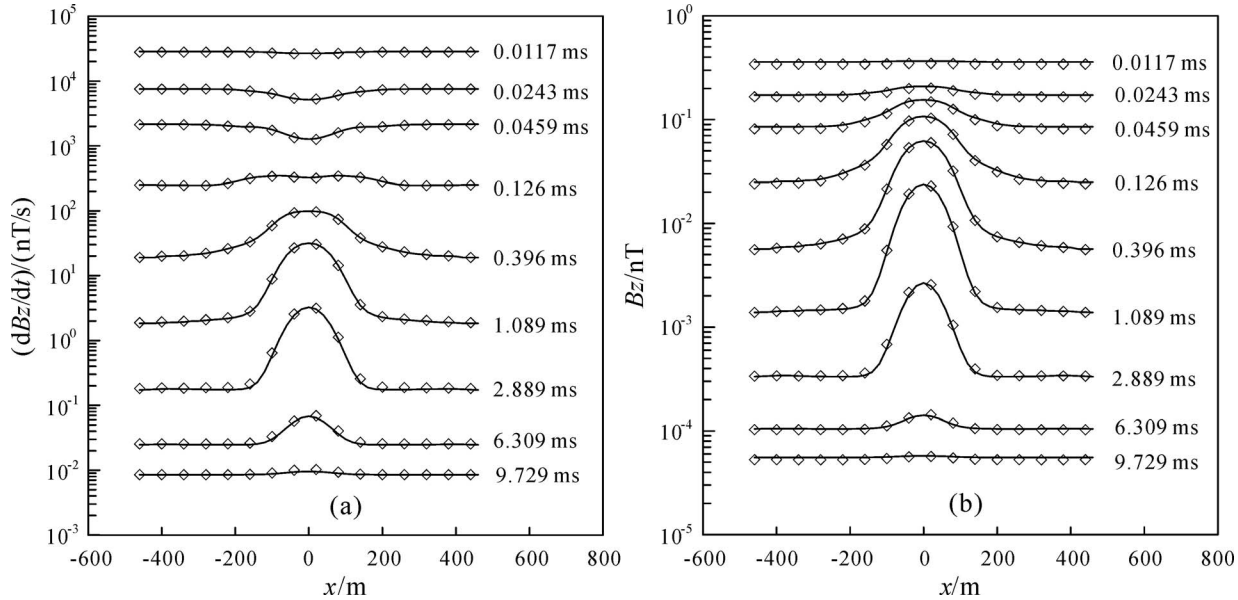


Figure 5. EM responses in profile from the separation method (solid lines) and total-field method (diamonds).

will be vastly reduced. Yang and Oldenburg (2016) used only 60 time steps ranging from 0.1 to 100 ms to complete the parallel computation. For airborne EM survey with moving transmitter and receiver and dense samplings, the time saved by the separation method is considerable. It will also benefit the future EM inversions.

As we know, the modeling accuracy is influenced by the grid size. Large cell size only describes a rough EM propagation, especially when the calculation area is close to transmitters. This may result in losing important information at early time channels for shallow earth, reducing the modeling accuracy. To study the influence of the grid size of EM responses, we show in Fig. 6 modeling results for different cell sizes (25 m and 50 m). The model is the same as in Fig. 3. From the figure, one sees that our separation method has a high accuracy for both cell sizes. For the total-field method, however, the results with 25 m cell size agree relatively well with those of FE method, but the results with 50 m cell size separate from those of the FE method, especially at the early time channels. In summary, with separation

method of this paper, we can use a relatively large grid size to obtain accurate model results. In other words, the separation method has a high modeling efficiency.

EM Responses for Complicated Underground Structures

Multiple Geological Bodies

To further show the feasibility of our algorithm, we first assume a model with multiple abnormal bodies. Refer to Fig. 7, there are totally four geological bodies, the upper two are located at 50 m deep with resistivity of 2,000 $\Omega\cdot m$ and 10 $\Omega\cdot m$, respectively, while the lower two bodies are located at the depth of 190 m with the resistivity of 1 $\Omega\cdot m$ and 5,000 $\Omega\cdot m$, respectively. We have calculated the time-domain responses at the transmitter-receiver location for different time channels to study the EM diffusion characteristics.

To clearly demonstrate the influence on EM responses from different abnormal bodies, we take the ratio of EM field containing the geological bodies to that of a homogeneous half-space. Figures 8 and 9 show the planar view of the ratio of dB_z/dt and B_z for different off-time channels. From Fig. 8, one sees the same decay pattern for conductors as in Fig. 5(a). In fact, from the left side of the figure, the EM signal decays from 0.00873 ms to 0.0189 ms, indicating the influence from the top resistive body. Then, from 0.0189 ms to 0.0783 ms, the EM signal decreases, indicating the combined influence from the top resistive body and the underlying conductor. From 0.0783 ms to 14.49 ms, it increases to

Table 1. Time consumption for separation and total-field method.

Method	t_f (s)	t_s (s)	n_f	n_s	N_{tx}	Running time (min)
Total-field method	4.2	0.07	5	500	47	43.87
Separation method	0.7	0.02	5	500	47	10.58

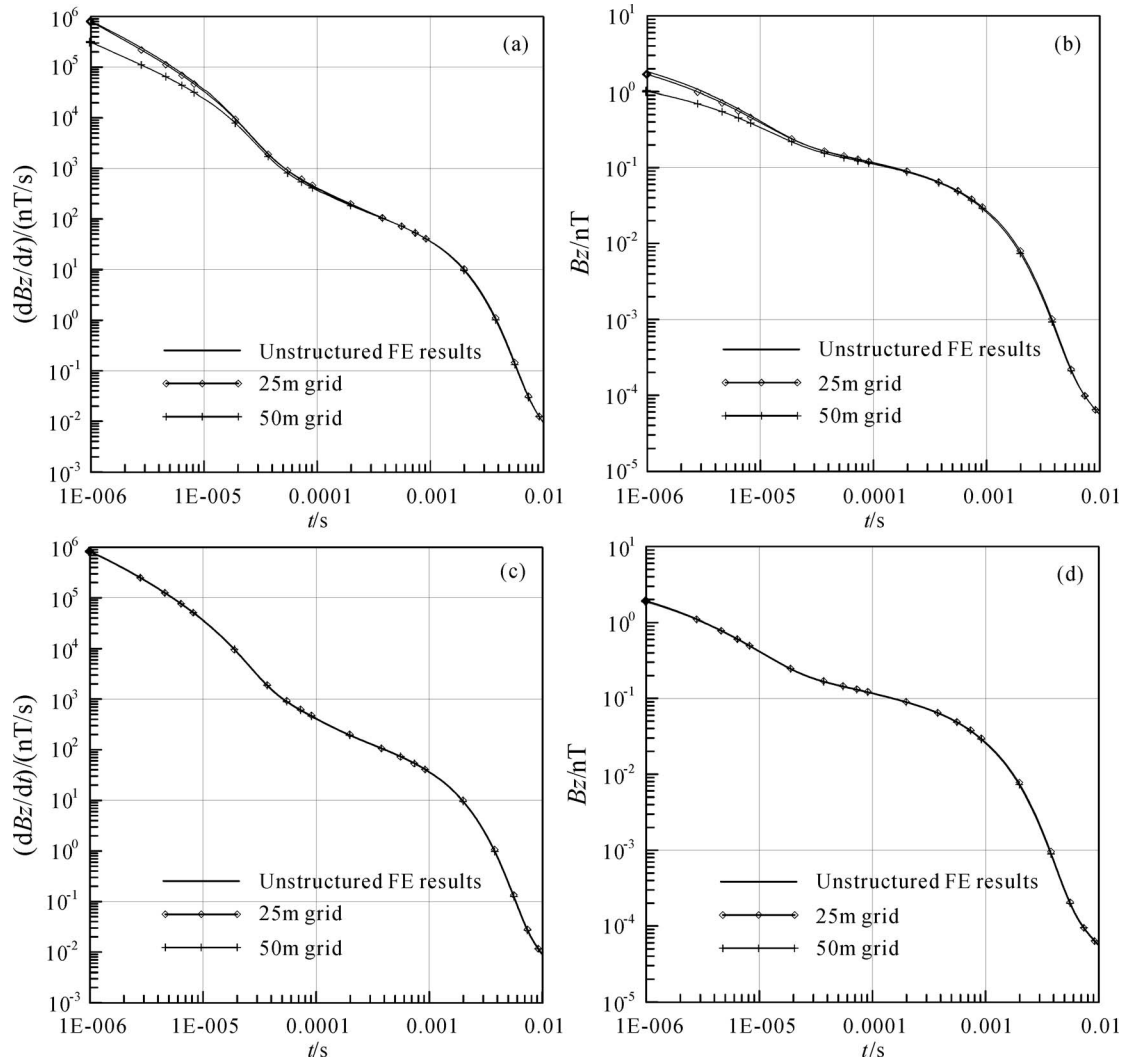


Figure 6. Comparison of EM responses for different grid sizes. (a) (b) are results of total-field method, while (c) (d) are results for the separation method.

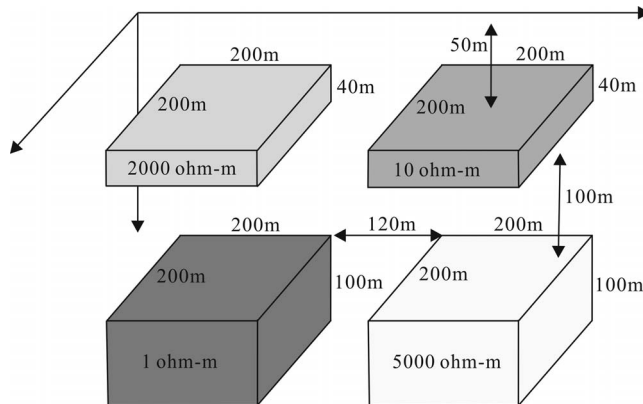


Figure 7. Multiple geological bodies embedded in a homogeneous half-space.

the maximum and then decreases until vanishing at very late time. This implies the dominant influence from the deep conductor. For the right side, as the conductor is located at the shallow earth, the EM signal decreases at early time 0.00873 to 0.0189 ms, and then increases from 0.0189 ms, reaches maximum at 0.45 ms, and finally it decays to zero at very later time channel. The influence from the deep resistive body is very small due to shielding effect from the top conductor.

Similarly, Fig. 9 shows that B_z demonstrates the same pattern for conductors in Fig. 5(b). The magnetic field on the left side decreases from 0.00837 ms to 0.0783 ms, indicating the influence of the top resistive body. It then increases to maximum and then decreases again until vanished, indicating the influence from the deep conductor. On the right side, the conductor is located at the shallow earth, the magnetic field increases

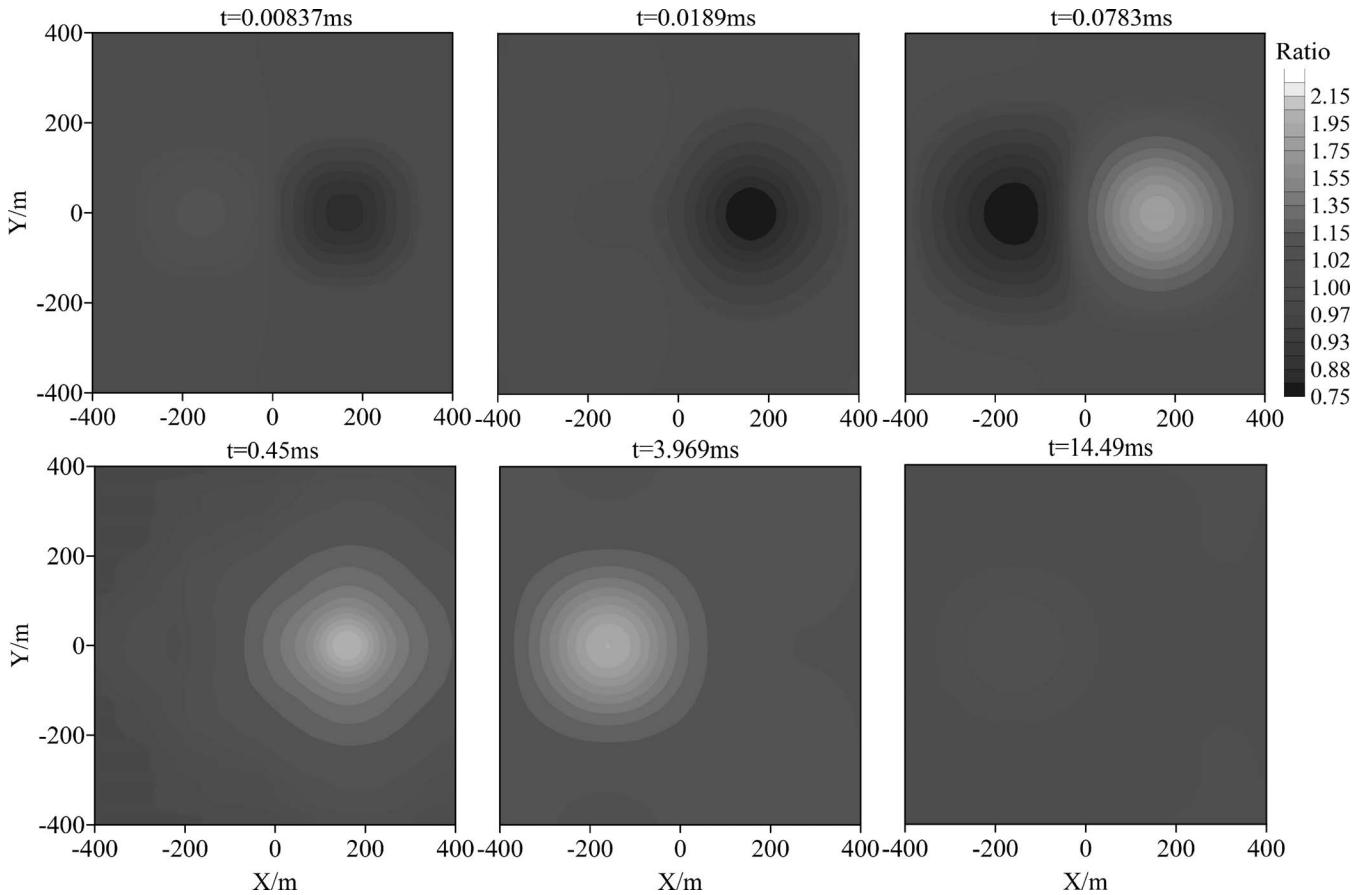


Figure 8. Planar view of dB_z/dt for different off-time channels.

with time and then decreases until vanished. The deep resistive body is similarly shielded by the top conductor.

Fracture Zone

The airborne EM is effective tool for groundwater exploration. Thus, in this section we study the EM responses for a conductive fracture in the earth (Fig. 10). The overburden has a resistivity of $100 \Omega\cdot\text{m}$ and a thickness of 20 m. The fracture zone is 40m in width, 180 m along the trending direction and 100 m in vertical. The resistivity of fracture is $10 \Omega\cdot\text{m}$. The surrounding rock has a resistivity of $1,500 \Omega\cdot\text{m}$. The grids used for this model is shown in Fig. 11.

We establish a coordinate system with the origin located at the ground projection of the fracture center, y-axis along the strike direction and the x-axis along the profile. Figure 12 shows the EM responses for different time channels. From the figure, one can see the general feature for a conductive body. While for the present model of a dipping fracture, the anomaly at each time channel leans toward the dipping direction, indicating well the inclination of the fracture zone.

Validity for an Arbitrary Transmitting Waveform

Until now, we have only considered the step transmitting wave. As airborne EM systems can transmit different kinds of waveforms such as the triangular, square, half-sine, and trapezoid etc. A flexible modeling method suitable for these complex transmitting waves becomes very important. The separation method presented in this paper can easily simulate the EM responses for different transmitting waves, because only for the primary field one needs to consider the transmitting wave and then the secondary field will automatically contain the waveform information via Eq. (8). In the following, we take a half-sine transmitting wave as example to discuss the flexibility of our separation method.

According to Yin *et al.* (2008), the primary electric field for a half-sine transmitting wave can be obtained from a convolution of step wave field and the derivative of transmitting current, *i.e.*,

$$\mathbf{E}_p(t) = -\frac{d\mathbf{I}(t)}{dt} * \mathbf{E}_{\text{step}}(t). \quad (18)$$

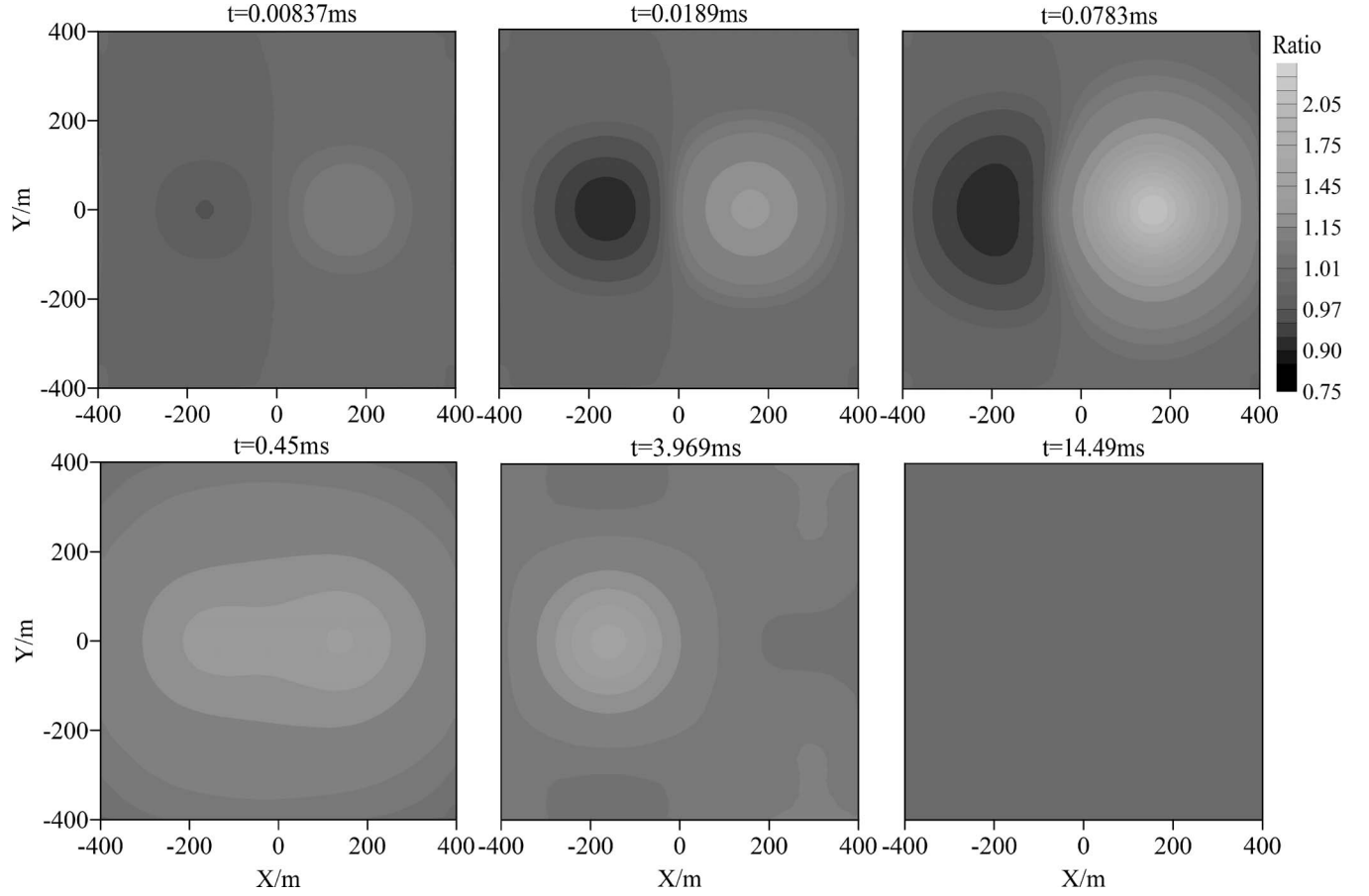


Figure 9. Planar view of B_z for different off-time channels.

The convolution in Eq. (18) can be calculated by Gaussian quadrature (Yin *et al.*, 2013), *i.e.*,

$$\int_a^b f(x)dx = \frac{b-a}{2} \sum_{i=1}^N w_i f\left(\frac{b-a}{2}x_i + \frac{a+b}{2}\right), \quad (19)$$

where x_i and w_i are respectively Gaussian sample coordinates and the corresponding weighted coefficients. After obtaining the primary electric field, we can follow the same procedure as before to calculate the EM

response for arbitrary transmitting waves without necessity to reconsider the transmitting wave.

We calculate the EM responses for the same model as Fig. 3 and use local mesh 1 in our modeling. The half-sine wave has a pulse width 4 ms, off-time 16 ms, and a transmitting current 10 A. Figure 13 shows the full-time (on- and off-time) EM responses for the model, while Figs. 14 and 15 show the EM responses in profile. From the figure, one sees that all off-time signal decays with time. For the on-time signal, a clear correlation exists between the profile and the time decay signal. Among them, dB_z/dt from both the profile and the time decay the signal decreases from a positive value to zero, changes polarity and increases until reaching a maximum. Then it decays again until the pulse width when the off-time starts. In comparison, the B -field increases until reaching a maximum, and then decreases to zero. After polarity change, the signal increases until the pulse width and starts the off-time decay. From the on-time responses, we also find the fact that the locations of sign reversal of the EM signal correspond to the edges of the underground abnormal body.

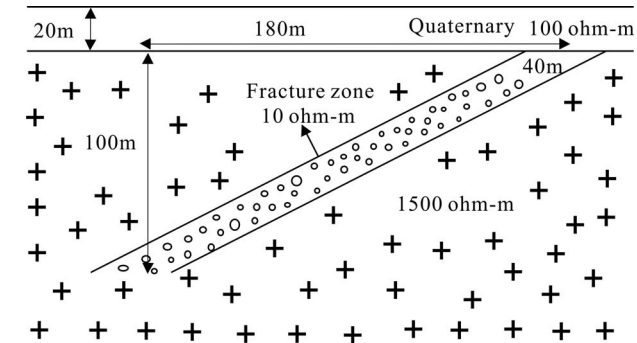


Figure 10. Fracture zone model.

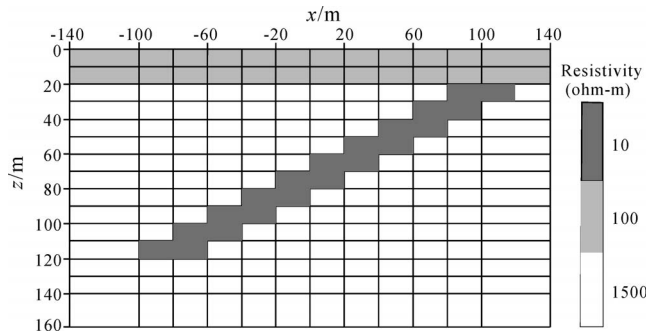


Figure 11. Grids around the fracture zone.

Conclusions

By exploiting the merits of different techniques, we have successfully developed a fast, effective, and accurate algorithm for 3D AEM modeling for complicated media and arbitrary transmitting waveforms. Among them, the FV method can model complicated structures with high accuracy; the separation approach for secondary field avoids the numerical singularity near the transmitting source and are suitable for modeling arbitrary transmitting waveform; the direct solver conducts factorization only once for the same time

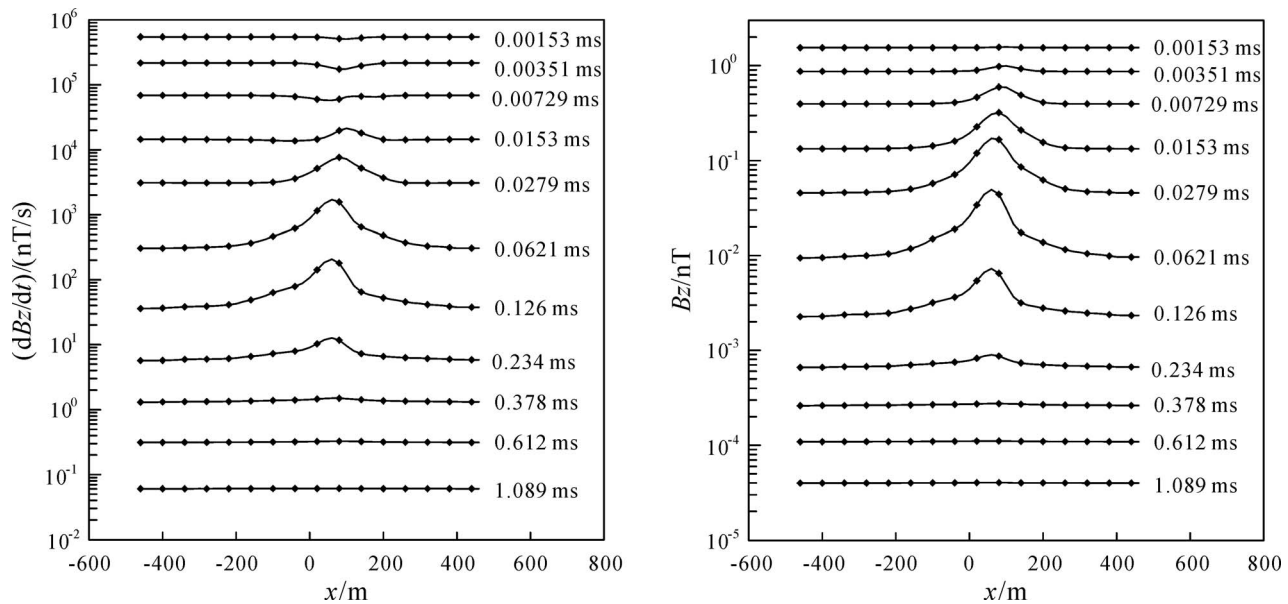


Figure 12. AEM responses of the fracture zone for different time channels.

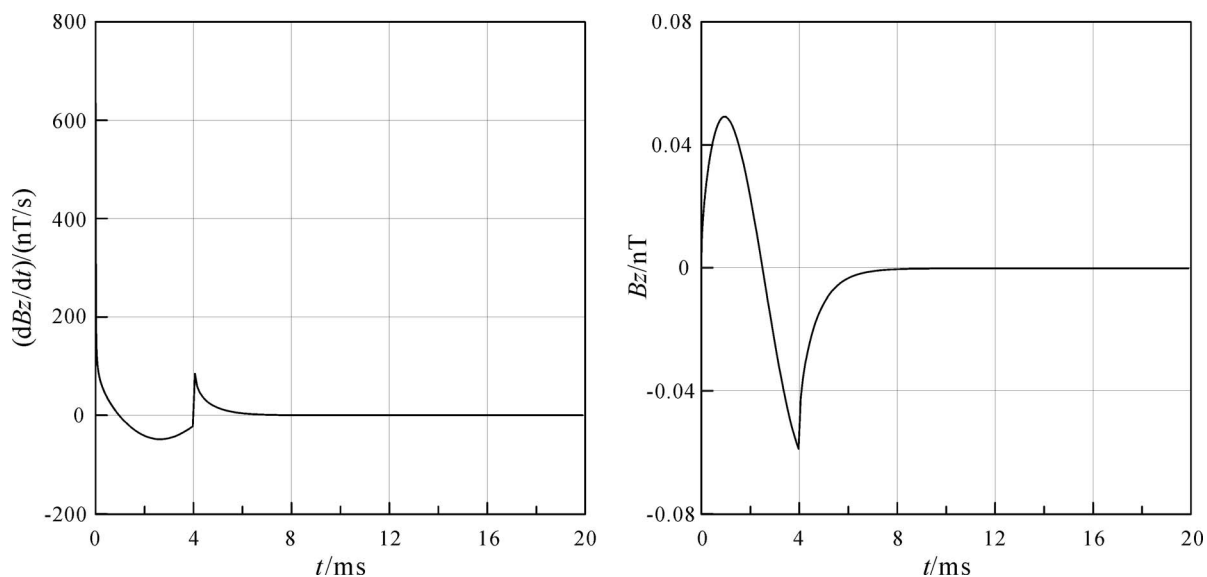


Figure 13. AEM responses for the model in Fig. 3 for a half-sine transmitting wave.

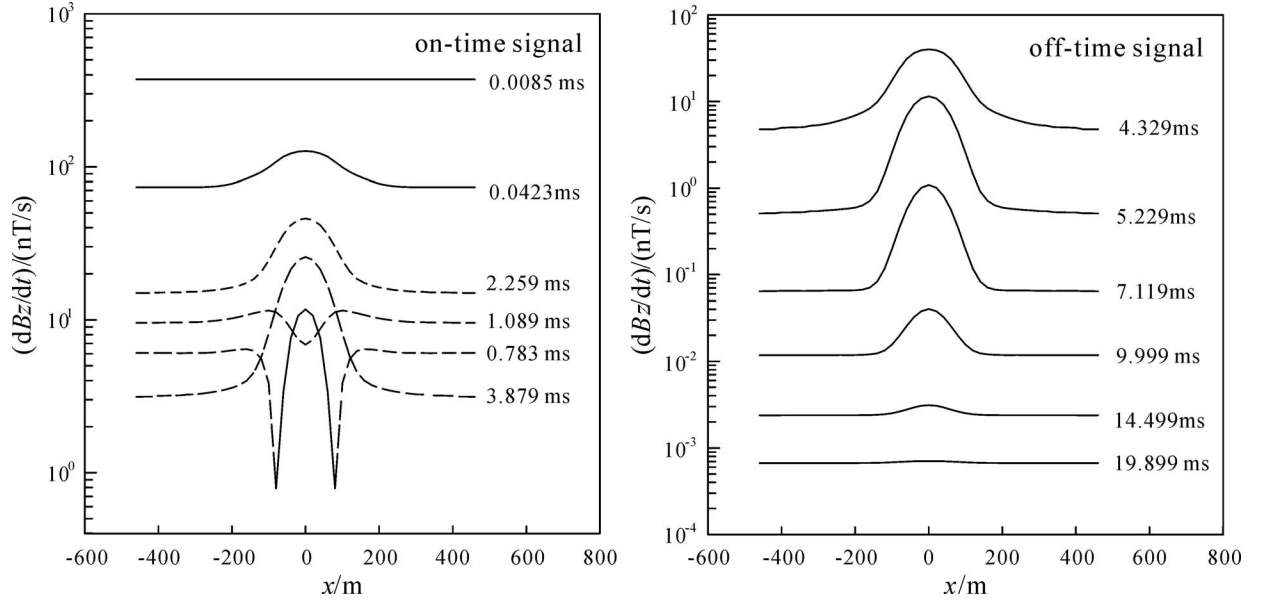


Figure 14. dBz/dt responses in profile for the model in Fig. 3 for a half-sine transmitting wave. The dashed lines are for negative values.

steps; while the local mesh reduces the time cost. With all these techniques, the 3D modeling algorithm developed in this paper can save up to 75.9% time compared to the total-field method and is less influenced by the grid size. This is extremely important for airborne EM due to its large data amount and moving transmitter and receiver. The simulation for different transmitting waveforms and complicated underground structures like fracture zone demonstrates its effectiveness and effi-

ciency. We hope that the fast modeling can help establish an efficient 3D time-domain AEM inversion procedure. This will be our future research focus.

Acknowledgments

This paper is financially supported by Key Program of National Natural Science Foundation of China (41530320) and Natural Science Foundation (41274121), China Natural Science Foundation for Young Scientists (41404093), Key National Research

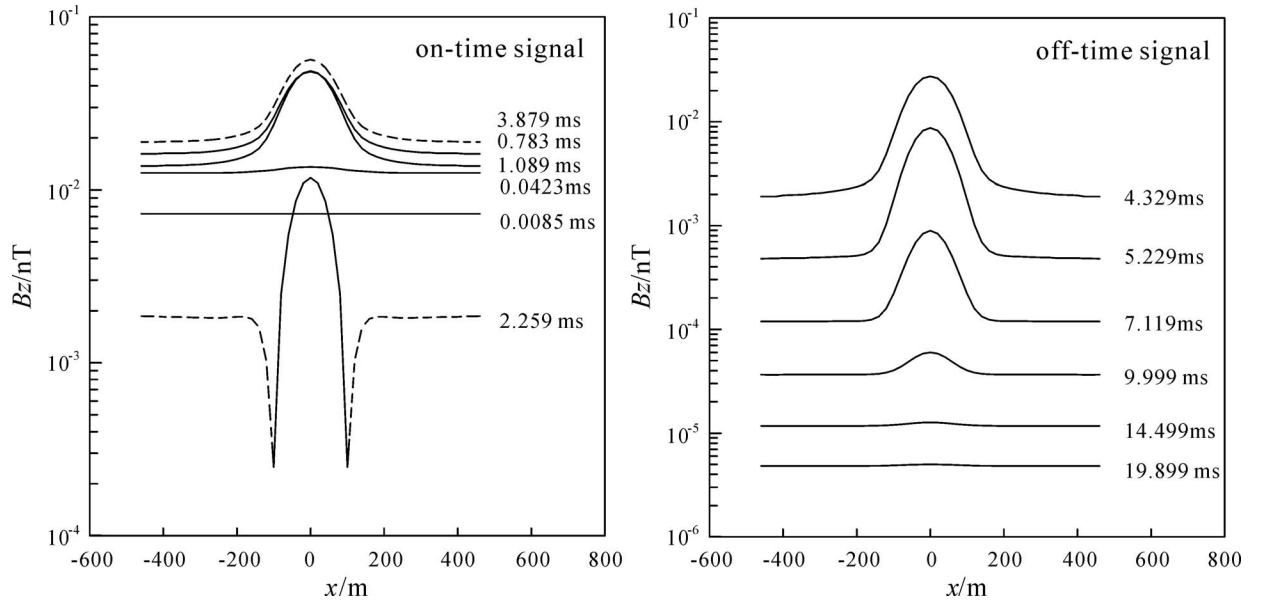


Figure 15. Bz responses in profile for the model in Fig. 3 for a half-sine transmitting wave. The dashed lines are for negative values.

Project of China (2016YFC0303100, 2017YFC0601903), Project 2017033 Supported by Graduate Innovation Fund of Jilin University, Projects on the Development of the Key Equipment of Chinese Academy of Sciences (ZDYZ2012-1-03).

References

- Amestoy, P.R., Duff, I.S., L'Excellent, J., and Koster, J., 2001, A fully asynchronous multifrontal solver using distributed dynamic scheduling: *SIAM Journal on Matrix Analysis and Applications*, **23**, 15–41.
- Christensen, N.B., 1990, Optimized fast Hankel transform filters: *Geophysical Prospecting*, **38**, 545–568.
- Commer, M., and Newman, G.A., 2004, A parallel finite-difference approach for 3-D transient electromagnetic modeling with galvanic sources: *Geophysics*, **69**, 1192–1202.
- Cox, L.H., and Zhdanov, M.S., 2007, Large scale 3D inversion of HEM data using a moving footprint: 77th Annual International Meeting, SEG, Expanded Abstracts, 467–471.
- Cox, L.H., Wilson, G.A., and Zhdanov, M.S., 2010, 3D inversion of airborne electromagnetic data using a moving footprint: *Exploration Geophysics*, **41**, 250–259.
- Haber, E., 2014, *Geophysical electromagnetics*: SIAM.
- Jahandari, H., and Farquharson, C.G., 2014, A finite-volume solution to the geophysical electromagnetic forward problem using unstructured grids: *Geophysics*, **79**, E287–E302.
- Oldenburg, D.W., Haber, E., and Shekhtman, R., 2008, Forward modelling and inversion of multi-source TEM data: 78th Annual International Meeting, SEG Expanded Abstracts, 559–563.
- Oldenburg, D.W., Haber, E., and Shekhtman, R., 2013, Three dimensional inversion of multisource time domain electromagnetic data: *Geophysics*, **78**, E47–E57.
- Operto, S., Virieux, J., Amestoy, P., L'Excellent, J., Giraud, L., and Ali, H.B.H., 2007, 3D finite-difference frequency-domain modeling of visco-acoustic wave propagation using a massively parallel direct solver: A feasibility study: *Geophysics*, **72**, SM195–SM211.
- Sasaki, Y., and Cho, S., 2011, 3D finite-difference modeling of time-domain electromagnetic data for mineral exploration: *Proceedings of the 10th SEGJ International Symposium*, Kyoto, Japan.
- Um, E.S., Harris, J.M., and Alumbaugh, D.L., 2010, 3D time-domain simulation of electromagnetic diffusion phenomena: A finite-element electric-field approach: *Geophysics*, **75**, F115–F126.
- Wang, T., and Hohmann, G.W., 1993, A finite-difference time-domain solution for three-dimensional electromagnetic modeling: *Geophysics*, **58**, 797–809.
- Xu, Y.C., Lin, J., Li, S.Y., Zhang, X.S., Wang, Y., and Ji, Y.J., 2012, Calculation of full-waveform airborne electromagnetic response with three-dimension finite-difference solution in time-domain: *Chinese Journal of Geophysics*, **55**, 2015–2114.
- Yang, B., Xu, Y.X., He, Z.X., and Sun, W.B., 2012, 3D frequency-domain modeling of marine controlled source electromagnetic responses with topography using finite volume method: *Chinese Journal of Geophysics*, **55**, 1390–1399.
- Yang, D., and Oldenburg, D.W., 2016, Survey decomposition: A scalable framework for 3D controlled-source electromagnetic inversion: *Geophysics*, **81**, E69–E87.
- Yang, D., Oldenburg, D., and Haber, E., 2013, Massive parallelization of 3D electromagnetic inversion using local meshes: 5th International Symposium on Three-Dimensional Electromagnetics, Sapporo, Japan.
- Yee, K.S., 1996, Numerical solution of initial boundary problem involving Maxwell's equations in isotropic media, *IEEE Transactions on Antennas and Propagation*, **14**, 302–307.
- Yin, C.C., Huang, W., and Ben, F., 2013, The full-time electromagnetic modeling for time-domain airborne electromagnetic systems: *Chinese Journal of Geophysics*, **56**, 3153–3162.
- Yin, C.C., Ren, X.Y., and Liu, Y.H., 2015, Exploration capability of airborne TEM systems for typical targets in the subsurface: *Chinese Journal of Geophysics*, **58**, 3370–3379.
- Yin, C., Smith, R., and Hodges, G., 2008, Modeling results of on- and off-time B and dB/dt for time-domain airborne EM systems: 70th Annual EAGE Conference and Exhibition, Extended Abstract, Rome, 1–4.
- Yin, C., Qi, Y., Liu, Y., and Cai, J., 2016, 3D time-domain airborne EM forward modeling with topography: *Journal of Applied Geophysics*, **134**, 11–22.
- Zhao, Y., Wang, Y.P., and Li, X., 2015, Study of 3-D ATEM modeling including surface topography based on FDTD method: 2015 Near Surface Asia Pacific Conference, 71–74.
- Zhu, K.G., Lin, J., Han, Y.H., and Li, N., 2010, Research on conductivity depth imaging of time domain helicopter-borne electromagnetic data based on neural network: *Chinese Journal of Geophysics*, **53**, 743–750.